THERMALLY INDUCED VIBRATIONS OF THE HUBBLE SPACE TELESCOPE'S SOLAR ARRAY 3 IN A TEST SIMULATED SPACE ENVIRONMENT

Derrick A. Early[1], William B. Haile[1], Mark T. Turczyn[2]

[1]*Swales Aerospace, 5050 Powder Mill Road, Beltsville, Maryland 20705 USA, Email: dearly@swales.com*
[2]*NASA GSFC, Mailstop 442.0, Greenbelt, Maryland 20771 USA, Email: mturczyn@hst.nasa.gov*

ABSTRACT/RESUME

NASA Goddard Space Flight Center and the European Space Agency (ESA) conducted a disturbance verification test on a flight Solar Array 3 (SA3) for the Hubble Space Telescope using the ESA Large Space Simulator (LSS) in Noordwijk, the Netherlands. The LSS cyclically illuminated the SA3 to simulate orbital temperature changes in a vacuum environment. Data acquisition systems measured signals from force transducers and accelerometers resulting from thermally induced vibrations of the SA3. The LSS with its seismic mass boundary provided an excellent background environment for this test. This paper discusses the analysis performed on the measured transient SA3 responses and provides a summary of the results.

1   INTRODUCTION

This year during the Hubble Space Telescope (HST) servicing mission 3B (SM3B), NASA astronauts will install Solar Array 3 (SA3) on HST. This will replace the nearly 7 year old Solar Array 2. The SA3 will provide more power with less surface area by using Gallium Arsenide Solar Cells mounted on honeycomb panels. NASA expects the new SA3 to provide power to HST for the remainder of its mission. Fig. 1 illustrates how HST will appear after SM3B.
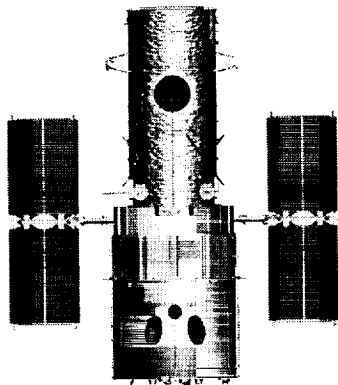

Fig. 1 HST with Solar Array 3 Installed

To qualify for flight on HST, a test was designed to verify that the SA3 would not disturb the HST after installation. NASA called this test the Disturbance Verification Test (DVT) of Solar Array 3. The test objective was to measure thermally induced vibrations of SA3 in a test simulated space environment. The events of interest were transient vibrational responses. It was mandatory to measure these vibrations if they had been large enough to cause Loss of Lock (LOL) on the HST guide stars. [1]

To conduct this test, NASA Goddard Space Flight Center (GSFC) used the European Space Agency (ESA) Large Space Simulator (LSS) in Noordwijk, The Netherlands. This chamber was the best in the world for providing thermal, vacuum and solar simulation with a dynamically quiet seismic mass boundary. As shown in Fig. 1, SA3 consists of two wings. NASA placed one of the flight wings in the LSS on a stiff pedestal and rotated the wing 49 degrees to the solar beam. This rotation and the 2.9 m tall pedestal was necessary to position the wing for full illumination by the solar simulator with its 6 m beam. Fig. 2 shows the SA3 flight wing mounted on the pedestal. The 656 lb SA3 spans a width of 7.6 m and a height of 4.1 m above the top of the pedestal.

The testing was conducted over four days using two shifts to cover 24 hours per day. After contamination bakeout and thermal equilibrium, the LSS simulated 20 orbital cycles. During the orbit simulations, data acquisition systems measured 40 hours of signals from instrumentation. This paper describes the methodology used to screen the data to find any thermally induced vibrations of the SA3 wing.

2   INSTRUMENTATION

For this test, the instrumentation consisted of accelerometers, force transducers, thermocouples, a vacuum gage and solar sensors. Fig. 2 shows the location of the accelerometers with labels a1 through a7. All of the locations had three axes instrumented with the exception of a5. Only the X_{sa} and Z_{sa} axes were instrumented at a5.
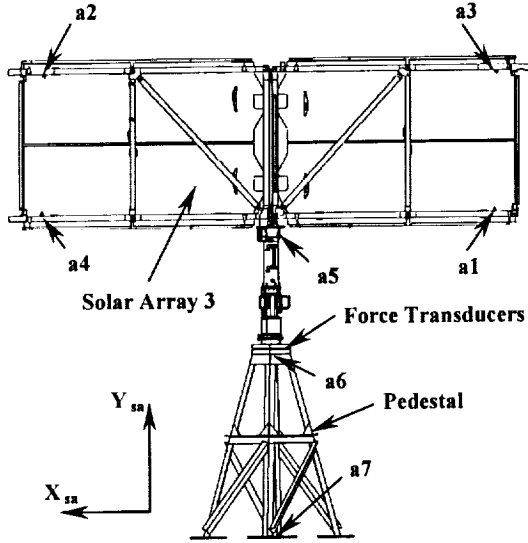
Fig. 2 Flight Solar Array 3 on Test Fixture

Fig. 3 shows the locations of the four force transducers located at the top of the pedestal. They are labelled f11 through f14. Each force transducer produced three orthogonal force signals oriented in the pedestal coordinate system. Two of the pedestal axes are labelled X_{ped} and Z_{ped} with X_{ped} pointing away from the sun simulator. The 131° angle between the SA3 and pedestal coordinate systems is shown. Eight of the force transducer signals were collinear; therefore, the signals were summed before the charge amplifier. This reduced twelve force signals down to a total of eight.
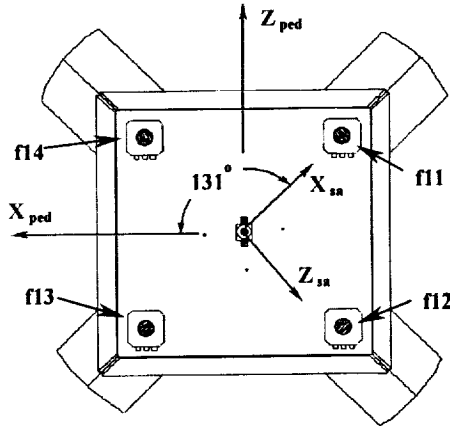

Fig. 3 Force Transducers

Fig. 4 shows the installation of the force transducers. They were sandwiched between an aluminum plate and the top of the stainless steel pedestal. A bolt through the center of the transducer was torqued while monitoring the force signal from the transducer. This technique allowed each bolt to be preloaded to 2000 lb.
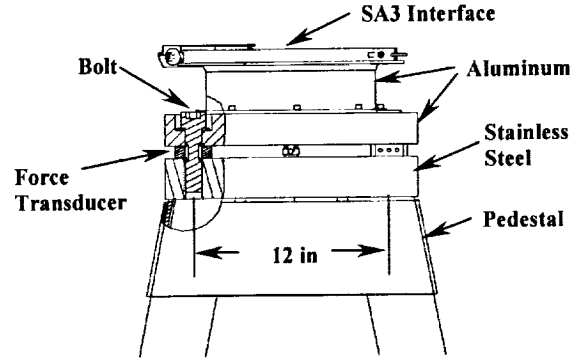

Fig. 4 Force Transducer Installation

3 SIGNAL PROCESSING

All of the primary and secondary bending and torsion modes of the SA3 exist between 1 and 10 Hz. Therefore, the data was band pass filtered in the following manner. An 8th order digital filter removed background noise above 10 Hz from the measured data with parameters set to emulate an analog elliptic low pass filter. Then, a 4th order digital filter removed transducer noise below 1 Hz with parameters set to emulate a Butterworth high pass filter. Application of these filters is described in [3].

The energy of the filtered signals y_i may be described in relation to a mean square value, Ψ_i^2, on p. 14 of [2]. This is simply the average of all the squared values in the time history as shown in Eq. 1. Table 1 contains filtered signal results of Eq. 1 for the two hour long 13th orbit simulation. Table 1 uses units of milli-pounds (mlb) and micro-g's (µg).

$$\Psi_i^2 = \lim_{T \to \infty} \frac{1}{T} \int_0^T y_i^2(t)dt \qquad (1)$$

In order to find short duration non-stationary events, Eq. 2 defines a short period average over time T to estimate the mean square values as a function of time.

$$\hat{\Psi}_i^2(t) = \frac{1}{T} \int_{t-T/2}^{t+T/2} y_i^2(t)dt \qquad (2)$$

Using the square roots of Eqs. 1 and 2, Eq. 3 normalizes the root mean square time histories of the filtered signals.

$$\overline{\Psi}_i(t) = \hat{\Psi}_i(t) / \Psi_i \qquad (3)$$

Table 1 Orbit 13 Signal Root Mean Square (rms)

Label	Axis	Ψ_i (mlb)	Label	Axis	Ψ_i (μg)
f11 + f14	X_{ped}	14	a1	X_{sa}	73
f12 + f13	X_{ped}	8	a1	Y_{sa}	95
f11 + f12	Z_{ped}	11	a1	Z_{sa}	85
f13 + f14	Z_{ped}	13	a5	X_{sa}	62
f11	Y_{ped}	76	a5	Z_{sa}	107
f12	Y_{ped}	29	a6	X_{sa}	17
f13	Y_{ped}	78	a6	Y_{sa}	14
f14	Y_{ped}	26	a6	Z_{sa}	16

4 SIGNAL SCREENING

With 40 hours of data to process, a screening method for finding significant events of short duration was needed. The background noise level was fairly stationary with little variation from orbit to orbit simulation. This is evident in Fig. 5 showing the minimum, maximum and mean of all the orbit simulation power spectral densities (PSD) for the Y axis signal of force transducer f14.
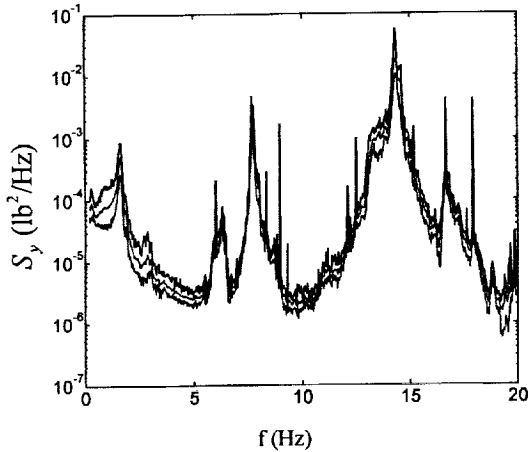
Fig. 5 PSD of Force Transducer f14 Y_{sa} Axis Signal

On p. 234 of [2], the reference suggests the use of short period mean square estimates to test for stationarity. In this analysis, time histories of normalized short period root mean square values were used in screening the data to uncover short duration events of non-stationarity.

In the following sections, three different screens were developed. The first simply looked for any force transducer signal exceeding an arbitrary threshold over the noise floor. Next, the double screen added the requirement that two force signals and two accelerometers must all exceed a threshold at the same

moment in time. This is reasonable, since any primary and secondary mode wing vibrations would result in multiple responses. Finally, the triple screen used the boundary accelerations measured at the top of the pedestal to analytically predict the force transducer signals resulting from chamber vibrations. Whenever the predicted force signals exceeded a threshold during an event found in the second screen, the event was removed from consideration.

4.1 First Screen

After computing $\overline{\Psi}_i$, these results were screened to find events that might cause HST to have a loss of lock event. For this screen, only the force transducer signals were examined. The screen flagged each time when any one of the signals had an upward crossing of threshold z. This screen can be described with Eqs. 4-7. Eq. 4 generates a threshold flag time history of ones when $\overline{\Psi}_i$ exceeds z and zeros otherwise. Eq. 5 sums all the force transducer threshold flag time histories to produce a time history that provides a count of all the force signals that exceeded z. Eq. 6 generates a screen logic time history of ones for the times when any one of the force signals $\overline{\Psi}_f$ exceeds z. Finally, Eq. 7 produces an up tick time history of only the rising transitions of p_1.

$$p_{si} = \begin{cases} 1 & \text{if } \overline{\Psi}_i(t) \geq z \\ 0 & \text{if } \overline{\Psi}_i(t) < z \end{cases} \quad (4)$$

$$p_f = \sum_{i=f} p_{si}(t) \quad (5)$$

$$p_1 = \begin{cases} 1 & \text{if } p_f(t) \geq 1 \\ 0 & \text{if } p_f(t) < 1 \end{cases} \quad (6)$$

$$p_{ei} = \begin{cases} 1 & \text{if } (p_i(t + \Delta t) - p_i(t)) > 0 \\ 0 & \text{otherwise} \end{cases} \quad (7)$$

The up tick p_{ei} time histories were summed for each of the orbit simulations. Table 2 lists a summary of the results of this screen. For a z of 4, a total of 25 events were found. These events were identified during the test using another methodology and were analyzed by HST pointing and control engineers. Their pointing and control system simulation results predicted no LOL for HST. This was very good news, and as a result the LOL disturbance requirement for SA3 was verified. In addition, the test objective was met.

In Table 2, orbit 13 was observed to be more active than the other orbits. This was also noticed during the

test. At the time, the engineers hypothesized that during an earlier orbit the activation of a heater on the aluminum interface plate, shown on Fig. 4, was the cause. Based on this hypothesis the test director disabled the heater.

Table 2 Maximum Force rms Events

orbit	Σp_e1(z) with T=1s				
	2.0	2.5	3.0	3.5	4.0
1	93	9	2	1	1
2	147	25	3	1	1
3	80	4			
4	147	14	1	1	1
5	134	20	7	3	2
7	181	18	4		
8	163	11	2	1	1
9	178	17	2		
10	89	9	2	1	1
11	174	8	1		
12	157	8	2	1	1
13	168	30	13	10	8
14	139	14	4	3	3
15	150	11	3	3	2
16	155	19	6	1	1
17	151	14	2		
18	164	15	3	3	3
Σ	2470	246	57	29	25

Fig. 6 contains time history plots of the maximum normalized rms signals grouped by SA3 accelerometers in the top plot, force transducers in the middle and boundary accelerometers in the bottom plot. The eight events counted in Table 2 for orbit 13 with a z of 4 can be seen clearly in the middle plot of Fig. 6. Notice that the major peaks on the top plot do not line up with the major peaks of the middle plot. Since the accelerometer and force transducer peaks did not correlate, they cannot be the result of SA3 vibrations.

4.2 Double Screen

Although the first screen identified no events that would cause LOL, any thermally induced vibrations were still interesting for their jitter effects. In a further attempt to find SA3 vibrations, this double screen was devised to find events with at least two force transducer signals and at least two SA3 accelerometer signals greater than z. Eqs. 4-9 define the screen. Eq. 8 sums all the SA3 accelerometer signals from a1 to a5 that have a $\overline{\Psi}_a$ greater than z. Eq. 9 defines the screen logic time history.

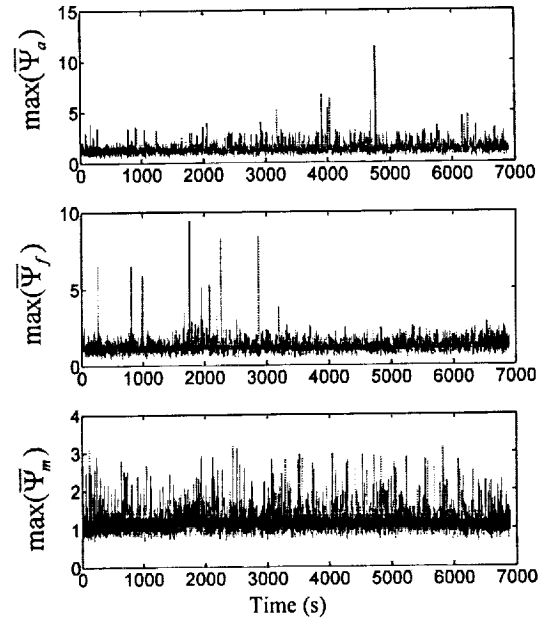$$p_a = \sum_{i=a} p_{si}(t) \qquad (8)$$

Fig. 6 Orbit 13 Normalized Signal rms

$$p_2 = \begin{cases} 1 & \text{if } p_a(t) \geq 2 \text{ and } p_f(t) \geq 2 \\ 0 & \text{otherwise} \end{cases} \qquad (9)$$

Table 3 summarizes the results of the double screen. The number of events with a z of 4 was reduced from 25 to only 2 events. All of these events occurred during the 5th orbit simulation.

Table 3 Double Screen Events

orbit	Σp_e2(z) with T=1s				
	2.0	2.5	3.0	3.5	4.0
1	42	3			
2	64	7			
3	41	3			
4	68	2			
5	70	13	4	3	2
7	87	10	3		
8	82	6			
9	94	10	4		
10	45	7	1		
11	74	4			
12	62	5			
13	92	6			
14	77	4			
15	79	6			
16	74	4			
17	82	6			
18	86	5			
Σ	1219	101	12	3	2

Fig. 7 plots the maximum $\overline{\Psi}_i$ time histories for 5th orbit simulation. Again, the top plot is the maximum of all the SA3 accelerometers. The middle is the force transducers, and the bottom plot is the seismic mass. The two events with a z of 4 are clearly evident on all three plots at 3500 and 4000 seconds. Since the seismic mass was moving, the SA3 responses were the result of base motion.
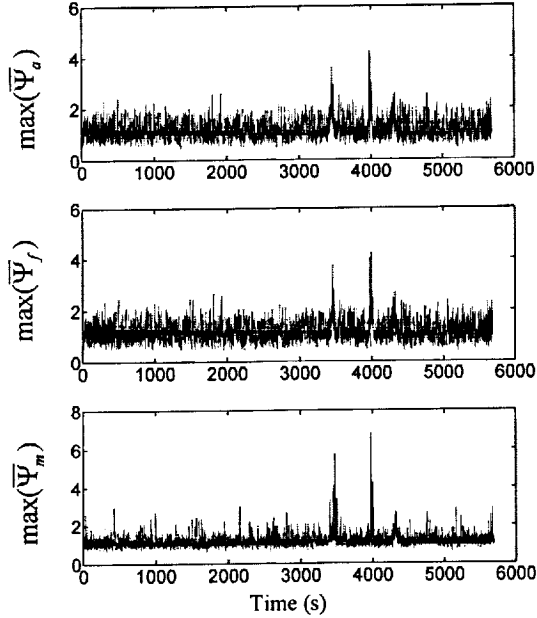

Fig. 7 Orbit 5 Normalized Signal rms

This assumption was verified by simulating impulse responses of the SA3. In the simulations, responses were observed on the accelerometers and the force transducers, but they were not observed on the top of the pedestal.

4.3 Triple Screen

In order to continue the search for thermally induced vibrations of the SA3, this third and final screen eliminates boundary excitation events by using a test data derived linear model to predict SA3 responses. A system identification of SA3 using the test data was performed and resulted in the A, B, C and D matrices contained in Eq. 10 for computing linear predictions of the SA3 responses $\hat{y}$. The methodology for performing the system identification is detailed in section 5.

$$\dot{x} = Ax + Bu$$
$$\hat{y} = Cx + Du \qquad (10)$$

For the final triple screen, the predicted force transducer responses were used in Eq. 11 to sum the number of $\overline{\Psi}_{pf}$ greater than z_p. Eq. 12 defines the logic time history. It is the same as the double screen with the added requirement on the predicted forces $\hat{y}_f$.

$$p_{pf} = \sum_{i=pf} p_{si}(t) \qquad (11)$$

$$p_3 = \begin{cases} 1 & \text{if } p_2(t) \geq 1 \text{ and } p_{pf}(t) \geq 1 \\ 0 & \text{otherwise} \end{cases} \qquad (12)$$

Table 4 lists the results from the triple screen. The number of events with a z of 2.5 was significantly reduced from 101 to a total of 4. On closer inspection of the time histories for these 4 events, they still appear to be caused by boundary motion. Therefore, no thermally induced vibrations of the SA3 were detected at z of 2.5.

Table 4 Triple Screen Events

orbit	$\Sigma p_{e3}(z)$ with T=1s and z_p=2				
	2.0	2.5	3.0	3.5	4.0
1	26				
2	42				
3	30	1			
4	45				
5	41				
7	52	1			
8	59				
9	56				
10	40				
11	59				
12	45				
13	66				
14	61	1			
15	57	1			
16	47				
17	63				
18	69				
Σ	858	4			

5   SYSTEM IDENTIFICATION

The triple screen above used predicted SA3 responses resulting from base excitation. In order to perform accurate predictions, a system identification was performed to estimate the state space matrices in Eq. 10. The elements of the matrices were cast into a modal parameter grey model form to be used in a parameter estimation algorithm detailed in [4].

Using the accelerometer signals from location a6 as an input source and all the other signals as output, the modal parameters were extracted from the test data.

Table 5 lists natural frequency and percent critical damping coefficient results from the system identification for both ambient and vacuum conditions. The right two columns contain the analytical frequency values from the finite element model of the test configured SA3 and critical damping coefficients from SA3 modal survey data for comparison.

Table 5 Modal Parameters

Mode	Ambient		Vacuum		Predicted	
	f_n	ζ	f_n	ζ	f_n	ζ
	(Hz)	(%)	(Hz)	(%)	(Hz)	(%)
1	1.2	3.1	1.3	4.7	1.1	4.7
2	1.5	4.4	1.7	4.6	1.4	3.9
3	-	-	1.8	3.0	1.8	2.3
4	5.3	0.2	5.5	0.4	5.2	1.7
5	6.2	0.9	6.4	1.4	5.9	1.4
6	6.3	0.9	6.6	0.6	6.5	1.7
7	7.4	1.0	7.8	0.7	7.5	1.6
8	12.9	0.7	13.7	1.9	12.9	2.4
9	13.9	2.7	14.6	0.8	13.4	2.9

5.1   Modal Parameter Grey Model

Eq. 13 represents the physical motion for the SA3. The degrees of freedom can be partitioned as shown in Eq. 14, where the x_b is the boundary and x_a are the interior degrees of freedom.

$$M\ddot{x} + C\dot{x} + Kx = F \tag{13}$$

$$\begin{bmatrix} m_{bb} & m_{ba} \\ m_{ab} & m_{aa} \end{bmatrix}\begin{Bmatrix} \ddot{x}_b \\ \ddot{x}_a \end{Bmatrix} + \begin{bmatrix} c_{bb} & c_{ba} \\ c_{ab} & c_{aa} \end{bmatrix}\begin{Bmatrix} \dot{x}_b \\ \dot{x}_a \end{Bmatrix} \\ + \begin{bmatrix} k_{bb} & k_{ba} \\ k_{ab} & k_{aa} \end{bmatrix}\begin{Bmatrix} x_b \\ x_a \end{Bmatrix} = \begin{Bmatrix} f_b \\ f_a \end{Bmatrix} \tag{14}$$

Substitute Eq. 15 into Eq. 14 and postmultiply by the transpose of the transformation. This Craig-Bampton transformation is described in [5].

$$\begin{Bmatrix} x_b \\ x_a \end{Bmatrix} = \begin{bmatrix} I & 0 \\ T_{ab} & \phi \end{bmatrix}\begin{Bmatrix} x_b \\ \xi \end{Bmatrix} \tag{15}$$

Assuming diagonal damping and no boundary damping coupling, Eq. 16 shows the results of the transformation.

$$\begin{bmatrix} \overline{m}_{bb} & m_{b\xi} \\ m_{\xi b} & I \end{bmatrix}\begin{Bmatrix} \ddot{x}_b \\ \ddot{\xi} \end{Bmatrix} + \begin{bmatrix} 0 & 0 \\ 0 & 2\zeta\omega_n \end{bmatrix}\begin{Bmatrix} \dot{x}_b \\ \dot{\xi} \end{Bmatrix} \\ + \begin{bmatrix} \overline{k}_{bb} & 0 \\ 0 & \omega_n^2 \end{bmatrix}\begin{Bmatrix} x_b \\ \xi \end{Bmatrix} = \begin{Bmatrix} f_b + T_{ab}^T f_a \\ \phi^T f_a \end{Bmatrix} \tag{16}$$

Since no interior forces f_a are applied the second row of Eq. 16 may be written as Eq. 17. If a thermally induced vibration event occurred, this assumption would be false momentarily; however, the averaging described in the next section will still make this a reasonable assumption.

$$\ddot{\xi} = -2\zeta\omega_n\dot{\xi} - \omega_n^2\xi - m_{\xi b}\ddot{x}_b \tag{17}$$

For the SA3, the boundary may be considered kinematic. Therefore, $\overline{k}_{bb}$ is zero, and the first row of Eq. 16 may be written as Eq. 18. Eq. 19 is formed by taking the second derivative of the second row of Eq. 15.

$$f_b = m_{b\xi}\ddot{\xi} + \overline{m}_{bb}\ddot{x}_b \tag{18}$$

$$\ddot{x}_a = \phi\ddot{\xi} + T_{ab}\ddot{x}_b \tag{19}$$

Finally, Eqs. 20 and 21 define the grey model state space matrices from Eqs. 17-19.

$$\hat{y} = \begin{Bmatrix} f_b \\ \ddot{x}_a \end{Bmatrix} \qquad x = \begin{Bmatrix} \dot{\xi} \\ \xi \end{Bmatrix} \qquad u = \ddot{x}_b \tag{20}$$

$$A = \begin{bmatrix} -2\zeta\omega_n & -\omega_n^2 \\ I & 0 \end{bmatrix} \qquad B = \begin{bmatrix} -m_{\xi b} \\ 0 \end{bmatrix}$$

$$C = -1 \cdot \begin{bmatrix} m_{b\xi}2\zeta\omega_n & m_{b\xi}\omega_n^2 \\ \phi 2\zeta\omega_n & \phi\omega_n^2 \end{bmatrix} \tag{21}$$

$$D = \begin{bmatrix} \overline{m}_{bb} - m_{b\xi}m_{\xi b} \\ T_{ab} - \phi m_{\xi b} \end{bmatrix}$$

5.2   Spectral Analysis

To estimate the modal parameters in Eq. 21, a spectral analysis of the data was performed. The objective was to compute frequency response functions using the boundary accelerations as a reference.

The power spectral density functions and cross spectral density functions in Eqs. 22 and 23 may be calculated from the cross-correlation function in Eq. 24, as on p. 435 in [6].

$$S_i(\omega) = \int_{-\infty}^{\infty} R_{ii}(\tau)e^{-i\omega\tau}d\tau \tag{22}$$

$$S_{ij}(\omega) = \int_{-\infty}^{\infty} R_{ij}(\tau)e^{-i\omega\tau}d\tau \qquad (23)$$

$$R_{ij}(\tau) = \lim_{T\to\infty} \int_{-T/2}^{T/2} y_i(t)y_j(t+\tau)d\tau \qquad (24)$$

In practice, the cross-correlation function in Eq. 24 is not calculated, and time cannot extend from $-\infty$ to $+\infty$. An approximation of the spectral Eqs. 22 and 23 is made by averaging methods detailed in [3] and [7].

Now the frequency response functions may be computed with Eq. 25, as in p. 162 of [2]. For this analysis, the input degrees of freedom, denoted by the subscript u, were the signals from accelerometer a6 shown in Fig. 2. Since only the translational accelerations were measured, S_{uu} is a three by three matrix at each frequency, ω.

$$H_{yu}(\omega) = S_{uu}^{-1}(\omega)S_{yu}(\omega) \qquad (25)$$

Eq. 26 computed the multi-input coherence C_y of the frequency response functions. The operator on the third term of the numerator in this equation takes transpose of the complex conjugate of H_{yu}. Eq. 27 computed the phase of the frequency response functions (FRF) by taking the imaginary part of its natural logarithm and converting to degrees. Fig. 8 shows a FRF plot of the force transducer f14 Y_{sa} axis signal referenced to the Z_{sa} axis of accelerometer a6.

$$C_y(\omega) = \frac{H_{yu}(\omega)S_{uu}(\omega)H_{yu}^*(\omega)}{S_y(\omega)} \qquad (26)$$

$$\phi_p = \frac{180}{\pi} \text{Im}(\ln H_{yu}) \qquad (27)$$

5.3 Modal Parameter Estimation

This section will describe how the parameters were computed to form the fit shown in Fig. 8. Using the FRF's computed by Eq. 25, impulse response functions in Eq. 28 were calculated by using the real portion of their inverse Fourier transformation. Then, the impulse response functions were truncated and trained together in Eq. 29. For the input signals, three impulses are defined in Eq. 30 where δ is the Dirac delta function.

$$h_{iu}(t) = \text{Re}\left(\int_{-\infty}^{\infty} H_{iu}(\omega)e^{i\omega t}d\omega\right) \qquad (28)$$

$$\tilde{y}_i = \left[h_{i1}(\tau) \; h_{i2}(\tau) \; h_{i3}(\tau)\right] \text{ with } \tau \in [0 \; T] \qquad (29)$$
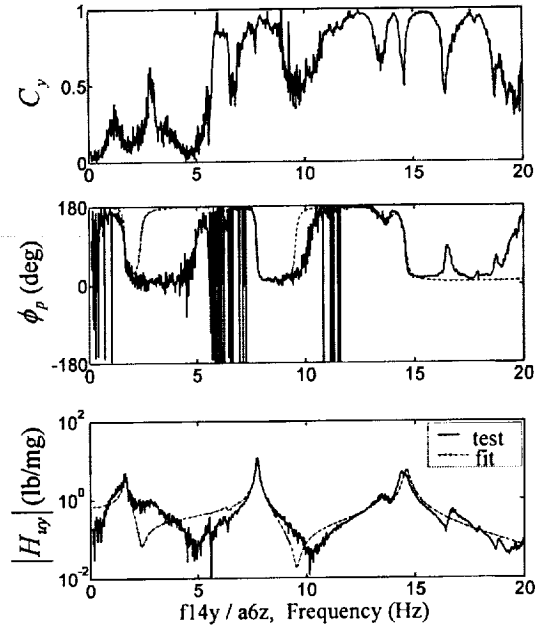

Fig. 8 Orbit 13 Force Signal FRF and Coherence

$$\tilde{u} = \begin{bmatrix} \delta(\tau) & 0 & 0 \\ 0 & \delta(\tau) & 0 \\ 0 & 0 & \delta(\tau) \end{bmatrix} \qquad (30)$$

Fig. 9 contains a plot of the impulse response functions computed for the three FRF's of the Y_{sa} axis force transducer signal from location f14 referenced to the three accelerometer signals from location a6.
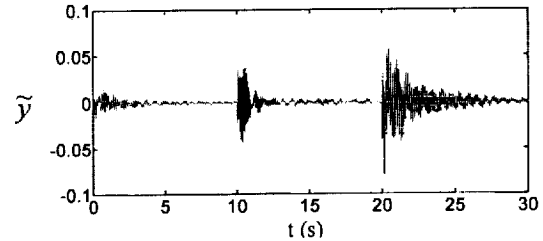

Fig. 9 Impulse Response Functions for f14 Y_{sa}

The state matrices in Eq. 21 are a function of the parameters contained in the parameter vector defined in Eq. 31. Here the elements in matrices ϕ, $\overline{m}_{bb}$, $m_{b\xi}$ and T_{ba} are reordered into single dimensioned vectors. Initial values for ζ, ω_n and ϕ are required to start the parameter estimation process.

$$\theta = \left[\zeta \; \omega_n \; \phi \; \overline{m}_{bb} \; m_{b\xi} \; T_{ba}\right] \qquad (31)$$

To obtain starting values of ζ and ω_n, a subspace method estimated a black box of the A, B, C and D

matrices with $\tilde{u}$ and $\tilde{y}_i$ as objective inputs and outputs, as in [4]. Then the complex eigenvalues, λ, of A were computed. The natural frequencies, ω_n, were computed from the magnitude of λ, and the critical damping coefficients, ζ, were computed by taking the negative cosine of the imaginary portion of the logarithm of λ in Eq. 32.

$$\omega_n = |\lambda| \qquad \zeta = -\cos(\text{Im}(\ln \lambda)) \qquad (32)$$

From these values, only reasonable results were retained. Then, Eq. 33 computed an initial value of ϕ by using the imaginary part of the peaks where j was selected to give the largest response at the natural frequency of ω_{nk}. The remaining parameters in θ may be started at zero.

$$\phi_{ik} = \text{Im } H_{ij}(\omega_{nk}) \qquad (33)$$

The state space matrices in Eq. 21 were estimated with a parameter estimation routine that minimizes the error between the predicted time history $\hat{y}$ and the impulse response functions $\tilde{y}$, detailed in [4]. Results of the parameter estimation are shown in Fig. 8 and in Table 5, and they are considered to be very good.

6 CONCLUSIONS

The disturbance verification test objective was to measure thermally induced vibrations of SA3 in a test simulated space environment. The events of interest were transient vibrational responses. It was mandatory to measure these vibrations if they had been large enough to cause Loss of Lock (LOL) on the HST guide stars. [1]

The objective of the test was met. Events were identified in the data. However, based on HST pointing control system simulations, no measured disturbances were large enough to cause the HST to experience LOL. Furthermore, many of the events identified by the first screen were not attributed to thermally induced vibrations of the SA3, since the accelerometer and force transducer signals did not correlate.

The double screen added the requirement that two force signals and two accelerometers must all exceed a threshold. This requirement was an attempt to eliminate noise on a single transducer signal from triggering and event. This screen found many events that were easily identified as boundary motion, since boundary motion will generate SA3 responses on both the force transducers and accelerometers.

Finally, the triple screen used the boundary accelerations to predict the force transducer signals. Whenever the predicted signals exceeded a threshold, the events were removed. The results of this final screen essentially eliminated all the events that were above the background levels. In other words, no thermally induced vibrations of the SA3 were detected above the background noise.

At this point in the analysis of the test data, no significant Solar Array 3 induced disturbances have been found in the test data that would impact the performance of the Hubble Space Telescope.

8 REFERENCES

1. Haile W. and Early D., Report of the Disturbance Verification Test of Solar Array 3, SAI-RPT-367, Swales Aerospace, 2001.

2. Bendat J. and Piersol A., *Random Data: Analysis and Measurement Procedures*, Wiley-Interscience, New York, 1971.

3. *Signal Processing Toolbox User's Guide*, The MathWorks, Inc., Nantick, Mass., 1988.

4. Ljung L., *System Identification Toolbox User's Guide*, The MathWorks, Inc., Nantick, Mass., 1988.

5. Craig R.R. Jr., and Bampton M.C.C., Coupling of Substructures for Dynamic Analysis, *AIAA Journal*, Vol. 6, No. 7, 1313-1319, July 1968.

6. Meirovitch L., *Elements of Vibration Analysis*, McGraw-Hill, New York, 1975.

7. Welch, P.D, The Use of Fast Fourier Transform for the Estimation of Power Spectra: A Method Based on Time Averaging Over Short, Modified Periodograms, *IEEE Trans. Audio Electroacoustics*, Vol. AU-15 June, 70-73, 1967.